Nano Research

Open Access

Research Article

Facile synthesis of hybridized Co/Fe-ZIF under solvent-free conditions for efficient oxidation evolution reaction electrocatalysis

YinSheng Xu[3,4], Zihan Li[1,4], Zhonghan Cheng[1,4], and Somboon Chaemchuen[1,2] ✉

[1] *State Key Laboratory of Advanced Technology for Materials Synthesis and Processing, Wuhan University of Technology, Wuhan 430070, China*
[2] *Department of Chemical Engineering, Faculty of Engineering, Mahidol University, Nakhon Pathom 73170, Thailand*
[3] *State Key Laboratory of Silicate Materials for Architectures, Wuhan University of Technology, Wuhan 430070, China*
[4] *School of Materials Science and Engineering, Wuhan University of Technology, Wuhan 430070, China*

Cite this article: *Nano Research*, **2025**, *18*, 94907022. https://doi.org/10.26599/NR.2025.94907022

ABSTRACT: Developing non-noble catalyst synthesis under green conditions with efficient electrochemical reactions is a challenging task in green energy technologies. To meet this challenge, the synthesis of hybridized non-noble cobalt and iron in the zeolitic-imidazole framework (Co/Fe-ZIF) through a solid-state thermal (SST) method is developed. In the obtained Co/Fe-ZIF structure, iron atoms are uniformly dispersed and randomly hybridized with primary cobalt atoms and imidazole linker, similar to the structure of ZIF-67. The hybridized Co/Fe-ZIF shows potential as an electrocatalyst for oxidation evolution reaction (OER). The optimal iron-incorporating catalyst, Co/$Fe_{0.2}$-ZIF, demonstrates remarkable performance with a minimized overpotential of 285 mV at the current density (*j*) of 10 mA·cm^{-2} in 1 M KOH. The synergistic effect of iron and cobalt ions on the catalyst provides active sites that bind to intermediate (OOH*) more strongly and facilitate high electron charge transfer, enhancing efficient electrocatalyst. Furthermore, the synergistic Co/$Fe_{0.2}$-ZIF catalyst demonstrates excellent durable reaction time compared to non-iron catalyst (ZIF-67) and conventional catalyst (RuO_2).

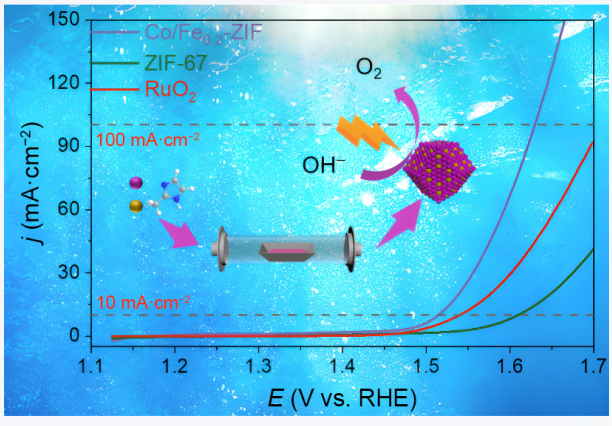

KEYWORDS: zeolitic-imidazole frameworks, solid-state thermal method, solvent-free synthesis, electrocatalyst, oxidation evolution reaction

1 Introduction

The energy crisis and more concerns about environment-relevant non-renewable sources derived from fossil fuels are significant motivations to explore new energy from renewable sources that are green and environmentally friendly [1–3]. To resolve this energy issue, electrochemical energy-related technologies such as water splitting, hydrogen production and fuel cells are alternative sustainability technologies that can potentially aspect and replace classical energy sources. Hydrogen production is considered the most straightforward and cleanest green energy source that can directly provide power for the future world while reducing our reliance on fossil fuels. Among the effective methods to obtain hydrogen, water electrolysis stands out as one of the most promising approaches [4, 5]. Water electrolysis or water splitting consists of two half-cell reactions, namely, oxygen evolution reaction (OER) and hydrogen evolution reaction (HER), which occurs on the anode and cathode side, respective, of the anion exchange membrane (AEM) combining the alkaline (ALK) and proton exchange membrane (PEM) technology [6–8]. Considering two half-cell reactions, the four proton and four electron coupled transfer between oxygen bond (O–O) in the half-cell OER is the kinetic rate of determining step, which requires the highest activation energy, leading to significantly limited hydrogen production efficiency [9, 10]. While precious metal catalysts such as RuO_2 are currently used as the trademark OER catalysts due to their high efficiency [11, 12]. However, their high prices, limited stability and selectivity make it challenging to use precious metal catalysts widely. Therefore, there is an urgent need to develop improved non-precious metal materials for the OER catalyst in renewable energy technologies [13, 14].

Received: July 5, 2024; **Revised:** August 9, 2024
Accepted: August 20, 2024

✉Address correspondence to sama_che@hotmail.com

Metal-organic frameworks (MOFs) are known as a new class of crystalline porous materials that have received significant attention due to their high surface area and porosity, showing enormous potential applications in various fields [15–17]. The diversity of metal clusters/ions and organic linkers to construct the framework on MOFs offers structural tunability in different properties. Moreover, the derivative carbon-based materials using MOFs as precursors or templates are further expanding on their potential applications [18–20]. Among MOFs, zeolitic-imidazole framework-67 (ZIF-67), composed of cobalt linked with imidazole ligands, has been widely explored as high crystalline, uniform distribution with dense metals, ultra-high surface area, large pore volume, stable structure, etc. In addition, the dense cobalt content on ZIF-67 provides promising potential for use as a catalyst for electrochemical application [21, 22]. The electrocatalytic activity and stability of cobalt in ZIF-67 and its derivative structures have been found to be higher than other transition metal elements [23, 24]. Up to date, there are several high-potential electrocatalysts based on ZIF-67 that have been developed and reported [25]. For instance, Anna Dymerska et al. [25] utilized ZIF-67 with Ni doping for efficient electrocatalytic OER under alkaline conditions with a low overpotential of 299 mV at 10 mA·cm^{-2}. Iron-functional electrocatalysts are also an excellent OER activity and are considered one of the best metal catalysts among other transition metals [26–28]. Dan Wen et al. synthesized an electrode with a multi-level heterogeneous structure of Material Institute Lavoisier-53 (MIL-53)@ZIF-67 and applied it as a catalyst for OER [29]. Notable, the iron-based metal bridged with a carboxylic ligand (terephthalic acid (BDC)) was the main structure in the framework of MIL-53. Their hybrid structures (MIL-53@ZIF-67) showed the performance under alkaline electrolytes at 10 mA·cm^{-2} with an overpotential of 193 mV. The Co-Fe synergy in the hybrid structure was found to promote electron transfer, significantly enhancing the inherent catalytic activity of catalytic sites and leading to excellent electrochemical performance. For a similar idea of hybridized materials, Dongyu Han et al. [30] enhanced the stability of the catalyst by constructing a yolk–shell structured FeCo-LDH@ZIF-67 (LDH: layered double hydroxide) composite material, resulting in an overpotential of 352 mV at 10 mA·cm^{-2} in 1.0 M KOH. Thus, the hybridizing or doping iron to prepare the bimetallic or composite Fe-Co MOFs bimetallic catalyst is a promising approach. However, their synthesized method is still a barrier to the synthesis of bimetallic or hybrid Fe/Co MOF electrocatalysts, such as the need for a multi-step process, time-consuming in crystallization or structural assembly, employed solvent during the synthetic process with consequently generated waste-solvent, etc. Therefore, a new synthetic process with a facile, green and environmentally friendly route is required to develop a synthesis electrocatalyst for efficient OER performance [31].

This work investigated a facile synthesis of hybridized cobalt and iron atoms in the zeolitic imidazole frameworks (Co/Fe-ZIF) through the novel solid-state thermal method (SST) to apply an efficient electrocatalyst of OER. The iron atoms were simultaneously integrated into the framework during the crystallization of ZIF-67 of the SST method, resulting in iron homogeneous hybridized and well-dispersed in the framework of Co/Fe-ZIF catalysts. Notable, the facile method and free-solvent participation in the SST method synthesized highly effective sites over Co/Fe-ZIF-67 catalysts, an advantage over the early reported method to synthesize iron functionalized ZIF-67 catalysts. Controlling the iron content in the physically mixed precursor could maximize the catalytic performance of Co/Fe-ZIF catalysts for OER. At a current density (j) of 10 mA·cm^{-2}, the significantly low overpotential of Co/Fe$_{0.2}$-ZIF is a much lower overpotential than that of the non-iron catalysts (ZIF-67 and trademark RuO_2). The synergy hybridized Fe/Co significantly functionalizes to modify the pristine ZIF-67 structure and increase the electrochemically active area. Notable, the solid-state thermal method (SST) for synthesizing ZIFs (ZIF-8 and ZIF-67) was first developed by our research team [32–34]. This method has an advantage as it directly uses the synthesized ZIFs for further applications without requiring post-treatment or activation. Significantly, the synthesis of hybridized metals in ZIF-67 through the SST method for efficient electrocatalyst of OER is first invented in this work. This catalyst was synthesized in a single step without adding solvents or additives. The residues and by-products were simultaneously removed during the synthesis process, which aligns with the principles of green chemistry aimed at minimizing the use of solvents and waste and reducing costs.

2 Experimental

2.1 Materials and synthesis

All chemical reagents/sources used in experiment are commercially available and directly used without further purification. The metal sources (cobalt(II) acetylacetonate (97%), iron(III) acetylacetonate (97%)), 2-methyl imidazole (98%), potassium hydroxide and the commercial RuO_2 were purchased from Shanghai Aladdin Bio-Chem Technology Co., Ltd.

In the synthesis of Co/Fe$_{0.2}$-ZIF, cobalt acetylacetonate (1 mmol, 257 mg), iron acetylacetonate (0.2 mmol, 70.6 mg) and 2-methylimidazole (2-MIM, 4.0 mmol, 328 mg) were physically ground under ambient conditions to obtain as a precursor. The solid precursor was placed into a ceramic boat (30 mm × 60 mm × 15 mm) and transferred to a muffle furnace (TL 1200, Nanjing Boyuntong Instrument Technology Co, Ltd.). The solid precursor was thermal treatment with the programmable controller under an inert carrier gas (Ar) flow rate of 50 cm^3·min^{-1}. The temperature program initially ramped up from room temperature to 100 °C within 30 min, followed by a further increase to 200 °C at a rate of 5 °C·min^{-1} and held at 200 °C for 1 h before naturally cooling down to room temperature. The obtained material, Co/Fe$_{0.2}$-ZIF, was directly used for further characterization and applications without post-treatment or purification. The different Fe loadings (Co/Fe$_y$-ZIF) were synthesized using a similar procedure to that of Co/Fe$_{0.2}$-ZIF. However, the mixed solid precursor was prepared by adding different proportions of iron(III) acetylacetonate (y: 5%, 20%, 35%, 50% mole based on 1 mmol of cobalt(II) acetylacetonate). The resulting materials were named Co/Fe$_y$-ZIF (y: 5%, 20%, 35% and 50%). It is worth mentioning that the synthesized Co/Fe$_y$-ZIF was directly used without post-treatment, purification, or activation.

2.2 Material characterization

The crystal structure was determined at room temperature using X-ray diffraction (XRD, Bruker D8 Advance). X-ray photoelectron spectroscopy (XPS) measurements were conducted using an ESCALAB 250Xi spectrometer with monochromatic Al Ka X radiation as the excitation X-ray source. Field emission scanning electron microscopy (FE-SEM, Zeiss Ultra Plus) were employed to

observe the morphology, size and elemental distribution of the materials. Nitrogen adsorption measurements at 77 K were used to determine pore volume and surface area (ASAP 2020). The materials were degassed (activated) at 180 °C under vacuum conditions for 3 h before further gas adsorption analysis.

2.3 Electrocatalytic oxygen evolution reaction (OER)

All electrochemical measurements were conducted by the AUTOLAB workstation electrochemistry. All electrochemical measurements were conducted in a standard three electrode system, with Pt as the counter electrode and Hg/HgO electrode as the reference electrode and the working electrode was a carbon paper coated with catalyst ink. The catalyst ink was prepared by mixing 5 mg of catalyst powder, 970 μL of anhydrous ethanol and 50 μL of Nafion solution and ultrasound for 30 min. Then 300 μL of ink was transferred to the surface of the carbon paper (1 cm^2) and then dried at room temperature to obtain the working electrode with a catalyst loading of 1.5 $mg{\cdot}cm^{-2}$. For comparison, RuO_2 (1.5 $mg{\cdot}cm^{-2}$) was also prepared by similar procedure.

In this study, the potentials measured vs. the Hg/HgO electrode were converted to the reversible hydrogen electrode (RHE) scale using the Nernst equation as follows

$$E_{RHE} = E_{Hg/HgO} + 0.059 \times pH + 0.098$$

where, E_{RHE} is the conversion potential relative to RHE, $E_{Hg/HgO}$ is the standard potential of Hg/HgO at 25 °C (0.098 V). That experimental measurement potential is relative to the Hg/HgO reference electrode.

In electrochemical measurements, the chronopotentiometry test is performed at current of 0.01 A to obtain a stable curve. After that OER linear scanning voltammetry is performed at a potential of 1.124–1.724 V vs. RHE (V_{RHE}) at 5 $mV{\cdot}s^{-1}$ scanning rate and 90% *IR* compensation (*I* represents current and *R* represents resistance) for all electrochemical data to compensate Ohmic for the loss. Electrochemical impedance spectroscopy (EIS) is performed in the frequency range of 105–0.01 Hz and at 0.6 V with an amplitude of 0.01 V. Cyclic voltammetry (CV) is performed at different scanning rates from 25 to 150 $mV{\cdot}s^{-1}$ and at potentials between 0.924 and 1.024 V_{RHE} to study the value of double-layer capacitance (C_{dl}). C_{dl} was obtained by mapping the difference between the positive electrode and negative electrode current density and the scan rate at 1.074 V_{RHE}. The stability testing is performed in 1.0 M KOH solution at 10 $mA{\cdot}cm^{-2}$.

3 Results and discussion

The Co/Fe-ZIF materials were synthesized through the solid-state thermal (SST) method without any solvent, as shown in Scheme 1. A mixture of iron(III) acetylacetonate, cobalt(II) acetylacetonate and 2-MIM was physically mixed to serve as a synthetic precursor. It is important to note that the well-mixed physically mixed precursor without any chemical reaction or transformation (Fig. S5 in the Electronic Supplementary Material (ESM)). Therefore, this initial step (the physically mixed precursor) is distinguished from the early solvent-free methods, such as the sonochemical or ball-mill method. The precursor was then subjected to the thermal process under absent oxygen conditions by argon flow. The resulting materials were directly used for application or characterization without any post-synthesis or watched process. To adjust the iron content of the Co/Fe_y-ZIF materials, different iron ratios (*y*) were used in the physically mixed precursor. The novel SST method for incorporating iron into the framework of ZIF-67 is advantageous due to its simplicity, solvent-free and eco-friendly process compared with previously reported synthesis methods [32]. Additionally, the absence of solvent in the SST method overcomes limitations related to metal solubility for achieving higher concentrations and more precise loading of the transitional metals. Moreover, various metal species can be induced into ZIFs through the SST method.

The obtained Co/Fe_y-ZIF materials were applied as a catalyst for the oxidation evolution reaction (OER). The OER performance was evaluated in a 1.0 M KOH electrolyte using a standard three-electrode system. For comparison, the commercial RuO_2 was also assessed, with all measured values corrected for 90% IR compensation. All materials were prepared as inks and drop casting on carbon paper to obtain self-supporting electrodes. The effect of different iron ratios (*y*) in the obtained Co/Fe_y-ZIF for electrocatalytic performance and kinetic reactivity was primarily investigated. Linear sweep voltammetry (LSV) measurements revealed the working potentials of Co/Fe_y-ZIF from the different iron loading (*y*), as shown in Fig. 1(a) and Movie S1 in the ESM. The hybridized iron and cobalt on ZIF revealed a significantly improved catalytic performance via indicated lower overpotential compared to the non-iron functionalized ZIF-67. Furthermore, the Co/$Fe_{0.2}$-ZIF catalyst provided the lowest overpotential of 285 mV in a 1.0 M KOH electrolyte, exhibiting the best OER performance at a current density of 10 $mA{\cdot}cm^{-2}$ (Fig. 1(b)). Significantly, this overpotential on Co/$Fe_{0.2}$-ZIF catalyst showed much effective potential than that of commercial RuO_2 (311 mV) and outperformed other reported ZIF-67 (Fig. 1(e)) and its derivatives as OER catalysts (details in Table S1 in the ESM).

The kinetic rate is an important factor in evaluating the efficiency of the OER catalyst, which could be determined by the Tafel slope. A small Tafel slope indicates a high kinetic rate of reaction. To study the OER kinetics of the Co/Fe-ZIF catalysts, the polarization curve was fitted to the Tafel equation by determining the Tafel slope, as shown in Fig. 1(b). The iron functionalized catalysts of Co/Fe_y-ZIF exhibited a smaller slope than the non-iron functionalized catalyst (ZIF-67 of 116 $mV{\cdot}dec^{-1}$) which was consistent with linear scanning voltammetry (LSV) measurements. Significantly, the Co/$Fe_{0.2}$-ZIF catalyst obtained the smallest Tafel slope of 75 $mV{\cdot}dec^{-1}$, indicating the highest OER catalytic dynamics among synthesized catalysts. Further investigation was carried out

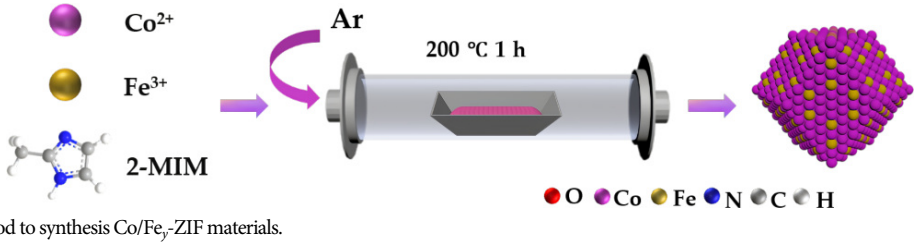

Scheme 1 The SST method to synthesis Co/Fe_y-ZIF materials.

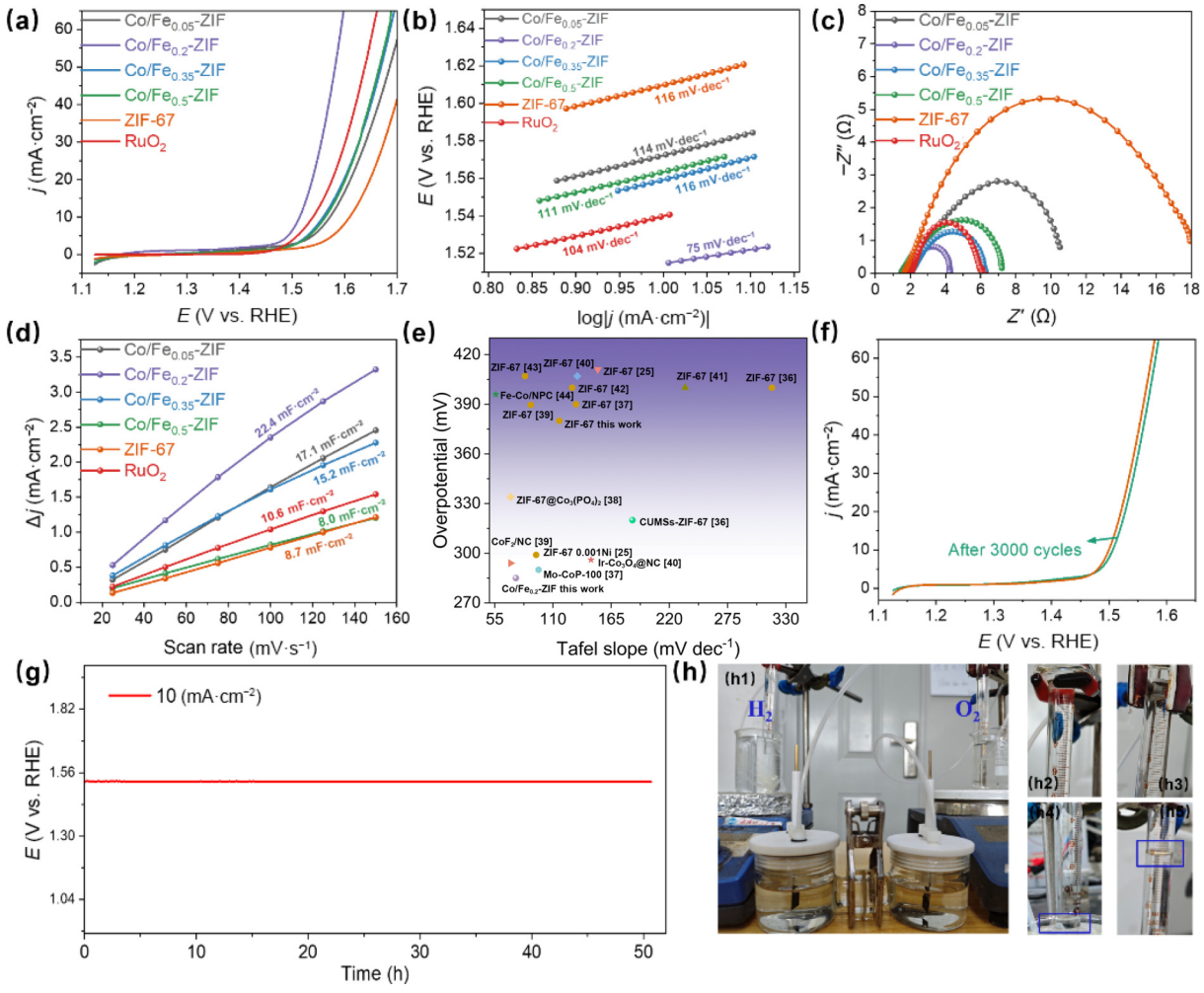

Figure 1 (a) LSV polarization curves of the synthesized Co/Fe$_y$-ZIF and RuO_2 under electrocatalysts of 1.0 M KOH solution. ((b) and (c)) The corresponding Tafel plots and EIS images from the LSV. (d) The capacitive currents as a function of scan rate. (e) The overpotential comparison of other report ZIF-67 [25, 36–44]. (f) Comparison before and after 3000 CV cycle. (g) Chronopotentiometry of Co/Fe$_{0.2}$-ZIF catalyst recorded at 10 mA·cm^{-2} for 48 h. (h) Diagram of drainage method device assembly. The gas correction before the reaction ((h2) and (h3)) and after the reaction ((h4) and (h5)) of O_2 and H_2, respectively.

to evaluate the possibility of charge transfer and the interfacial behavior of the electrocatalysts under OER conditions. These were measured by the electrochemical impedance spectrum (EIS). The corresponding Nyquist plot is analyzed to understand the conductivity of the catalysts. As expected, the hybridized iron/cobalt catalysts (Co/Fe-ZIF) showed enhancing conductivity (Fig. 1(c)) over the non-iron catalyst (ZIF-67). The improved conductivity of the hybridized Co/Fe-ZIF catalysts could significantly result in partial-charge transfer, activating the activating species and promoting the OER activity. Notable, the Co/Fe$_{0.2}$-ZIF catalyst exhibited the smallest charge transfer resistance (R_{ct}) and the lowest charge transfer impedance among the synthesized catalysts, which is consistent with other results of the catalytic OER performance.

The electrochemically active surface area (ECSA) of catalysts was positively correlated with their double-layer capacitance (C_{dl}), which was determined by CV at different scan rates. The C_{dl} value of the Co/Fe$_{0.2}$-ZIF catalyst was 22.4 mF·cm^{-2}, which was higher than that of the other catalyst, as shown in Fig. 1(d). This result showed that the Co/Fe$_{0.2}$-ZIF catalyst had a relatively higher surface roughness and more exposed active sites and indicated that moderate iron contents could increase the effective activation area (sites) of the electrode and improve its charge transfer. On the other hand, the C_{dl} value of the Co/Fe$_{0.5}$-ZIF catalyst was 8.0 mF·cm^{-2}. This result demonstrated that excessive iron content led to decreased structural stability. Stability is also a key indicator for evaluating electrocatalytic efficiency. The stability of the Co/Fe$_{0.2}$-ZIF catalyst was conducted in an alkaline solution and the result is shown in Figs. 1(f) and 1(g). The electrode potential of the Co/Fe$_{0.2}$-ZIF catalyst showed no significant change after several hours of continuous electrolysis at 10 mA·cm^{-2} current density, indicating the high durability of Co/Fe$_{0.2}$-ZIF catalyst. In addition, the LSV polarization curves of the Co/Fe$_{0.2}$-ZIF catalyst after 3000 CV cycles indicated nearly the overlap of original signals with maintaining performance (inserted Fig. 1(e)), which further confirmed the durable catalytic activity of the Co/Fe$_{0.2}$-ZIF catalyst toward the OER. In addition, the chronopotentiometry method for electrolysis at a current of 0.1 mA (shown in Fig. S4 in the ESM) was studied simultaneously. The drainage method was applied to collect the amount of H_2/O_2 to estimate the Faraday efficiency (FE) of the H-type electrolytic, as shown in Fig. 1(h). The Faraday efficiency was obtained to be up to 84% with the volume ratio of O_2 and the oxygen production reached about 6.4 mL after 902 s.

The obtained results indicate that the hybridized iron/cobalt in crystalline ZIF significantly improved the catalytic performance of

OER. The hybridized Fe and Co atoms in Co/Fe-ZIF catalysts cause electron charge rearrangement, generating more strongly active sites compared with the pristine ZIF-67 (no-iron catalyst). Consequently, intermediate products can be more efficiently adsorbed on active sites for catalytic conversion, maximizing the OER activity on Co/$Fe_{0.2}$-ZIF. Additionally, the induced iron atom catalysts improve electron transfer and conductivity, as was evident in the decrease in resistance (as seen in Fig. 1(c)). However, the excess iron portion in catalysts (Co/$Fe_{0.3}$-ZIF up to Co/$Fe_{0.5}$-ZIF) might compete with cobalt atom to coordinate with imidazole ligand (2-MIM). The weak crystallization was revealed when the iron ratio was increased in the precursor (see the discussion on catalyst characterization section). This weak crystallization resulted in decreased stability of catalysts. In addition, it can be observed that during the long-term activation process (chronopotentiometry), the electrolyte gradually turns brown and a layer of substance is loaded on the Pt electrode (Fig. S2 in the ESM). Therefore, we infer that the unstable structure may have degraded during the activated process, leading to a significantly increasing overpotential for OER performance. In addition, the exceeded iron content (> 20%) suggested in detachment phenomena in the electrolyte solution and the large amount of FeOOH produced during the catalytic process reduces the material's conductivity, thereby lowering the OER catalytic activity [35].

The hybridized iron and cobalt ions used to obtain the crystalline Co/Fe-ZIF affected the crystal structure and material properties were characterized and compared with the non-functionalized iron of ZIF-67. The different iron ratios (Co/Fe_y-ZIF, y: percentage mole ratio of iron to cobalt source) that affected the crystalline structure were initially analyzed by XRD. The diffraction pattern of initially induced iron obtained Co/$Fe_{0.05}$-ZIF revealed a similar diffraction pattern with ZIF-67, as shown in Fig. 2(a). It observed peaks at 7.4°, 10.4°, 12.8°, 14.7°, 16.4° and 18.1°, which corresponded the crystal planes (011), (002), (112), (022), (013) and (222), respectively, relative structure of ZIF-67 [45]. Further, those peaks with similar like diffraction pattern of ZIF-67 were obtained at raising iron ratios in the mixed precursor after normalized diffraction peak intensity. It could imply that the induced iron with ratios up to 50% Fe (Co/$Fe_{0.5}$-ZIF) provided the crystalline diffraction pattern and peak position (XRD) like diffraction pattern of ZIF-67 (non-iron incorporation). Although a similar peak position was observed on Co/$Fe_{0.5}$-ZIF, the crystal intensity on each peak provided a different ratio of peak intensity. The peak intensity at 7.4° gradually decreased with higher iron ratios in the mixed precursor. On the other hand, the opposite result was observed that exhibited higher peak intensities of 10.4° and 12.7° when more iron additional ratios. Moreover, the additional peak at 13.1° was observed on the highest iron percentage (Co/$Fe_{0.5}$-ZIF), which this peak was not observed at lower iron ratios used in the synthesis catalysts. Interestingly, this additional peak of 13.1° was matched to the primary diffraction of entirely replaced cobalt with iron source (Fe-MIM), as shown in Fig. S5 in the ESM. Nevertheless, the solid crystalline of Fe-MIM obtained a tiny size that could not perform the single-crystal analysis. It should be mentioned that the synthesized 100% iron ratio with 2-MIM under the solvothermal method (methanol as solvent) at room temperature also failed to obtain solid precipitation. Therefore, the results implied that the iron/cobalt ions hybridized to coordinate with imidazole liker (2-MIM) and their

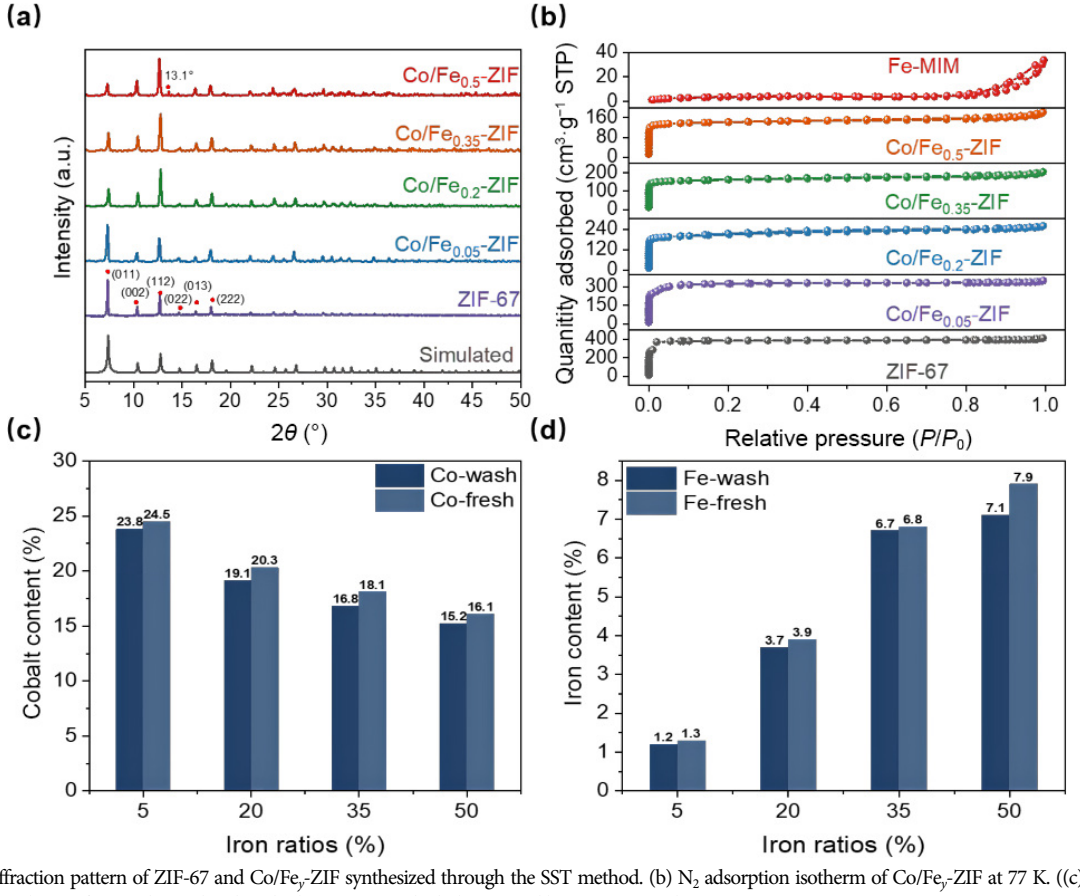

Figure 2 (a) Diffraction pattern of ZIF-67 and Co/Fe_y-ZIF synthesized through the SST method. (b) N_2 adsorption isotherm of Co/Fe_y-ZIF at 77 K. ((c) and (d)) Metal content of cobalt and iron of as-synthesized and washed Co/Fe_y-ZIF which determined by ICP-OES analysis.

crystal structure maintained a similar diffraction pattern with ZIF-67 but in different peak intensities. However, the excessing iron ratios in the precursor (such as Co/$Fe_{0.5}$-ZIF) resulted in a mixture of phase structures resembling ZIF-67 and Fe-MIM.

The porosity and surface area of Co/Fe-ZIF catalysts were measured by the N_2 adsorption–desorption at 77 K. The isotherm of Co/Fe_y-ZIF showed a sharp N_2 adsorption at relatively low pressure (P/P_0 < 0.05, P/P_0 is the equilibrium pressure divided by the saturation pressure), as shown in Fig. 2(b). These isotherm results were classified as N_2 isotherm Type I, representing the micropore structure is a primary pore in Co/Fe_y-ZIF catalysts. Consequently, the amount of N_2 adsorption on catalysts was used to calculate the specific surface area (Brunauer–Emmett–Teller (BET) and Langmuir), summarized in Table 1. The N_2 adsorption showed a relatively decreasing amount with the increasing iron proportions to induce in Co/Fe_y-ZIF catalysts. Consequently, the specific surface area indicated relatively decreasing with higher iron ratios (y) of Co/Fe_y-ZIF catalysts. Meanwhile, the pore volume also decreased with the increasing iron ratios of the catalysts. However, the average micropore size of Co/Fe_y-ZIF indicated increasing pore sizes with more iron ratios. The average micropore on Co/Fe_y-ZIF significantly increased with more iron ratios up to Co/$Fe_{0.2}$-ZIF (1.9852 nm), then showed a small change with further increasing iron ratios (Table 1). These results suggest that the iron ions competed with cobalt ions to coordinate with imidazole ligand (2-MIM) during the SST method to form crystallization of Co/Fe_y-ZIF.

However, the coordination configuration of iron with imidazole ligand (Fe–N coordination) is different from cobalt ions to coordinate with imidazole ligand (Co–N on ZIF-67). The different quality (diffraction pattern) and quantity (diffraction intensity) in the resulting diffraction of XRD (Fig. 2(a) and Fig. S1 in the ESM) were evident in the suggestion. The framework was terminated after the iron-coordinated imidazole ligand. The induced ions in the precursor terminated the growing framework and prohibited the crystallization, resulting in decreased crystallinity, surface area and pore development on Co/Fe_y-ZIF catalysts. Meanwhile, the iron-terminated coordination opened the micropore channel for larger pore sizes. Regarding electrochemical performance, the large surface catalyst with a well-dispersion of active species enhances the reactivity in the reaction. Meanwhile, the increased pore sizes promote the substrate mass transfer to active species and product diffusion. Optimizing the large surface area and pore size on Co/$Fe_{0.2}$-ZIF was suggested as one of the factors for obtaining maximized OER catalytic activity.

The content of cobalt and iron in Co/Fe_y-ZIF catalysts was measured by inductively coupled plasma-optical emission spectroscopy (ICP-OES). As depicted in Fig. 2(c), the cobalt content decreased with increasing iron ratios in the mixed precursor used to synthesize Co/Fe_y-ZIF. Conversely, the iron content showed an opposite trend, increasing with higher iron ratios in the mixed precursor (Fig. 2(d)). It is interesting to note that the total metal content (cobalt and iron) in the Co/Fe_y-ZIF catalysts remained relatively constant, closely matching the metal content of ZIF-67 (24.4 wt.%) cobalt from ICP-OES and 26.6 wt.% cobalt from the theoretical structure of Co(2-MIM)$_2$). It is important to mention that the cobalt source (1 mmol) and excess imidazole ligand source (4 mmol) were in constant proportion in the mixed precursor for synthesizing the Co/Fe_y-ZIF catalysts. Therefore, the ICP results indicated that the different induced iron ratios (y) did not influence the total metal content of the Co/Fe_y-ZIF. The excess imidazole ligand in the precursor was simultaneously eliminated by a carrier gas (Ar flow) during the SST method. The metal content analysis suggests that the induced iron competed with cobalt to coordinate with the imidazole ligand in a coordinated structure like ZIF-67. A similar diffraction pattern on Co/Fe_y-ZIF to ZIF-67 without the extra peak was used to confirm the suggestion.

Excess imidazole ligand in the mixed precursor over the theory structure and other residual sources may be present on Co/Fe_y-ZIF catalysts. To ensure the purity of the material, the catalysts were soaked in a solvent (dichloromethane) overnight to wash away the residual following conformation by the ICP analysis (denoted as washed Co/Fe_y-ZIF). The results showed that the cobalt and iron content in washed Co/Fe_y-ZIF was not significantly different from the metals content of as-synthesized Co/Fe_y-ZIF (Figs. 2(c) and 3(d)). However, the metal content in washed Co/Fe_y-ZIF was slightly higher than as-synthesize Co/Fe_y-ZIF with a low iron ratio in the precursor (Co/$Fe_{0.2}$-ZIF), possibly due to the tiny residual sources. Conversely, the metal (iron and cobalt) content slightly decreased in the high iron ratio between as-synthesized and washed Co/$Fe_{0.5}$-ZIF was suggested to be from uncoordinated metals. Furthermore, the weak coordination between metal and imidazole ligand in the framework of a high iron ratio might cause the leaching metals to dissolve in solvent (dichloromethane) during the washing process. This experiment confirms that the SST method can synthesize highly hybridized Co/Fe content up to 35% of Fe (Co/$Fe_{0.35}$-ZIF) in single-step without post-process. Additionally, the synthesis of hybridized Co/Fe-ZIF by the SST method provides the highest iron content with coordinated imidazole ligand over any previously reported synthesis through the solvent method [46, 47].

The surface morphology of catalysts was examined using SEM. According to the catalytic performance, the Co/$Fe_{0.2}$-ZIF was considered in surface morphology compared with the non-induced

Table 1 The specific surface area and porosity properties of Co/Fe_y-ZIF

Sample	Specific surface area ($m^2 \cdot g^{-1}$)		Pore volume[a] ($cm^3 \cdot g^{-1}$)	Pore width[a] (nm)
	BET	Langmuir		
ZIF-67	1639	1762	0.5918	1.2490
Co/$Fe_{0.05}$-ZIF	1304	1385	0.4172	1.6619
Co/$Fe_{0.2}$-ZIF	806	850	0.2367	1.9852
Co/$Fe_{0.35}$-ZIF	636	674	0.2057	1.9792
Co/$Fe_{0.5}$-ZIF	565	595	0.1858	1.9968
Fe-MIM	12	14	0.1498	2.1366

[a]Determined by the Horvath–Kawazoe method.

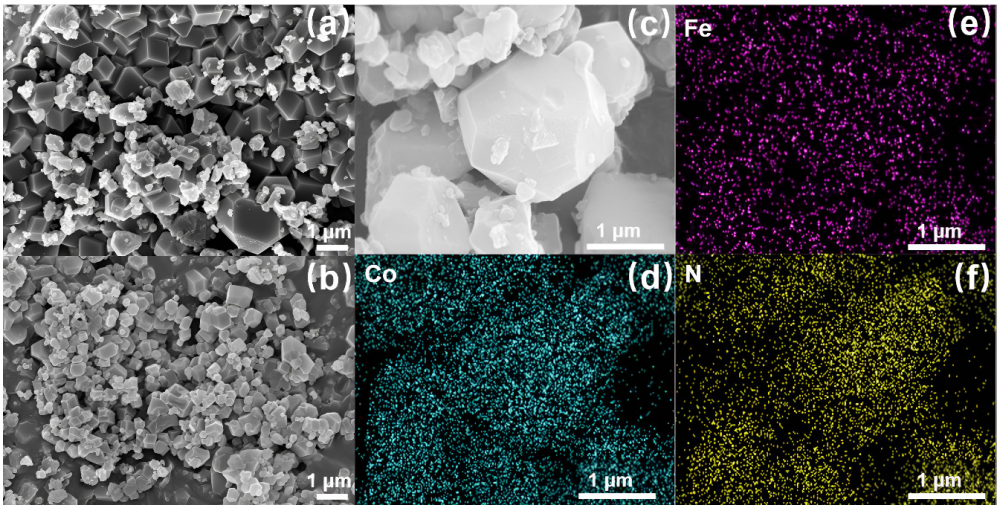

Figure 3 SEM images of (a) Co/$Fe_{0.2}$-ZIF, (b) ZIF-67 and ((c)–(f)) the SEM-EDS images of Co/$Fe_{0.2}$-ZIF.

iron catalyst (ZIF-67). An agglomerated rhombic dodecahedron structure with smooth crystal faces was observed on ZIF-67 and Co/$Fe_{0.2}$-ZIF, as shown in Fig. 3. The particle size ranged from approximately 100–500 nm. These observations are consistent with previous reports of thermal synthesis under solvent-free conditions [48]. However, the Co/$Fe_{0.2}$-ZIF catalyst contained a smaller crystal size than the ZIF-67 and exhibited non-perfect crystallization of the rhombic dodecahedron shape observed more on Co/$Fe_{0.2}$-ZIF than ZIF-67. This non-perfect surface morphology on Co/$Fe_{0.2}$-ZIF indicated that the hybridized iron in the framework affected the crystallization of Co/$Fe_{0.2}$-ZIF catalysts. The observed change in morphology on Co/$Fe_{0.2}$-ZIF was supported by the decreased crystallinity (XRD), surface area and porosity properties. Additionally, the elemental distribution on Co/$Fe_{0.2}$-ZIF was determined using energy-dispersive X-ray spectroscopy (SEM-EDS). The result showed that iron, cobalt and nitrogen are excellent dispersion without the agglomeration of elements on Co/$Fe_{0.2}$-ZIF. The mapping density revealed that the iron was lower than the cobalt element, consistent with the metal content analysis using ICP-OES. The chemical state and coordination geometry of catalysts was determined by XPS. The survey spectra showed the existing elements of the Co 2p, C 1s and N 1s regions on ZIF-67 and the additional peak of the Fe 2p region on Co/$Fe_{0.2}$-ZIF, as shown in Fig. 4(a). The binding energy of carbon C 1s at 284.8 eV was used to normalize the other element spectra. The deconvoluted high-resolution spectra of Co 2p displayed fitting peaks for Co $2p_{3/2}$ and Co $2p_{1/2}$ at around 781.0 and 796.8 eV and binding energies of satellite peaks at 785.5 and 802.8 eV indicating a divalent oxidation state of Co species on catalysts (Fig. 4(b)) [49]. The ZIF-67 and Co/$Fe_{0.2}$-ZIF were obtained a similar fitting peak of Co 2p. The deconvoluted N 1s spectra obtained two peaks at 397.7 and 400.8 eV, which represent the Co–N and C–N coordination, respectively (Fig. 4(c)) [29]. In addition, the C–N coordination on Co/$Fe_{0.2}$-ZIF catalyst revealed a slight shift to lower energy compared to the ZIF-67 catalyst. Interestingly, the ratio of two intensity peaks, Co–N (398.7 eV) to C–N (400.8 eV), on Co/$Fe_{0.2}$-ZIF was lower by about two times than that of ZIF-67. This result indicates the altered energy and strength of the original N coordination in the imidazole ligand, likely attributed to the binding energy of Fe–N coordination in Co/$Fe_{0.2}$-ZIF. In the high-resolution Fe 2p spectrum, the peaks at 712.2 and 724.0 eV were assigned to the characteristic peaks of the Fe^{3+} oxidation state in Co/$Fe_{0.2}$-ZIF (Fig. 4(d)) [50]. Interestingly, the XPS splitting of the Fe spectrum may imply the coordination of Fe^{3+} with N in the framework without altering the chemical species.

In general, OER electrocatalysts have the primary role of adsorbing reactants on the surface to form adsorption intermediates, thus facilitating charge transfer between electrodes and reactants [51]. OER consists of four basic processes

$$^{*} + OH^{-} \rightarrow OH^{*} + e^{-} \quad (1)$$

$$OH^{*} + OH^{-} \rightarrow O^{*} + H_2O + e^{-} \quad (2)$$

$$O^{*} + OH^{-} \rightarrow OOH^{*} + e^{-} \quad (3)$$

$$OOH^{*} + OH^{-} \rightarrow O_2 + H_2O + e^{-} \quad (4)$$

where the "*" represent the active species.

At the same time, to further understand the mechanism of electrochemical activation accelerated of Fe-Co bimetallic catalysts, Kai Ge et al. [52] revealed that the interaction between Fe-Co ions by density functional theory (DFT) calculation. The results show that MOF-Fe/Co has lower free energy relative to MOF-Co in OER process (Steps 1 and 2). This shows that iron incorporation is conducive to the adsorption and dissociation of intermediate products. Facilitates the rapid start of the OER process. Xianbiao Hou et al. [53] simulated the reaction path of the catalyst through DFT calculations. The results indicated that the interaction force between the surface-active sites of Co-MOF and the reaction intermediate (OOH*) was weak. The decrease in overpotential after doping Fe ions into Co-MOF proves that the reaction intermediate can be more easily adsorbed on the surface of the catalyst [54–56].

In order to explore the catalytic mechanism for OER, XPS was performed to investigate the changing elemental state on an as-synthesized and activated Co/$Fe_{0.2}$-ZIF catalyst. For the activated catalyst, the Co/$Fe_{0.2}$-ZIF catalyst performed the chronopotentiometry test for a period of time to obtain the active state following the XPS analysis (denoted activated Co/$Fe_{0.2}$-ZIF). The high-resolution Co 2p spectra significantly changed after the Co/$Fe_{0.2}$-ZIF catalyst activation. The Co^{2+} on as-synthesized Co/$Fe_{0.2}$-ZIF catalyst was shifted and split into a mixture of Co^{2+} and Co^{3+} on Co $2p_{3/2}$ peak (780.1 eV) and the Co $2p_{1/2}$ peak (795.1 eV) (Fig. 5(a)). In addition, the two satellite peaks (785.5 and 802.7 eV) of

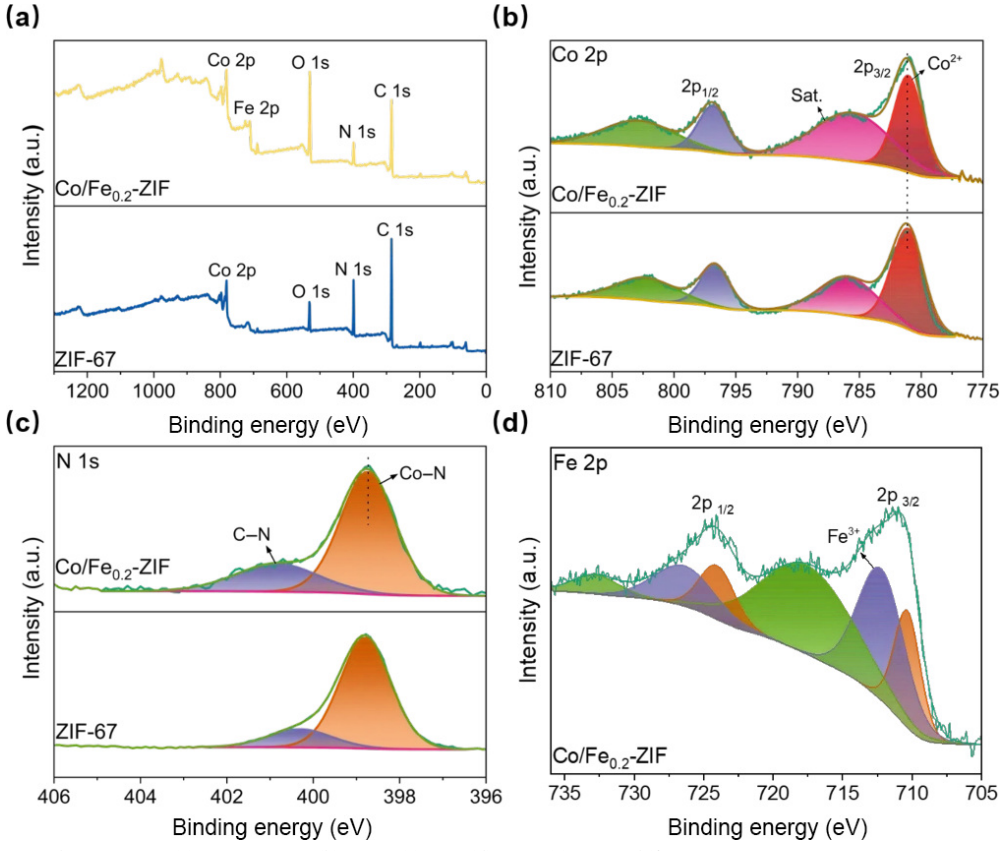

Figure 4 XPS of ZIF-67 and Co/$Fe_{0.2}$-ZIF: (a) survey spectra, (b) Co 2P, (c) N 1s, (d) Fe 2p, (e) O 1s and (f) C 1s.

cobalt species was decreasing intensity to nearly disappearing in the spectra of activated Co/$Fe_{0.2}$-ZIF catalyst. These results suggested a large proportion of Co^{2+} converted to Co^{3+} after activated catalyst. For the high-resolution Fe 2p spectra, the Fe^{3+} of the Fe $2p_{3/2}$ peaks was negatively shifted from 712.2 to 712.1 eV (Fig. 5(b)) owing to changes in the electronic structure of Fe species on the activated catalyst. In relevant result, the high-resolution Fe $2p_{3/2}$ peaks (712.1 eV) for Fe^{3+} revealed an increasing ratio, which was associated with the formation of FeOOH on the activated Co/$Fe_{0.2}$-ZIF catalyst [40, 57]. The high-resolution O 1s peaks (532.5 eV) for generated Fe-OH was observed as shown in Fig. S7 in the ESM. Therefore, the XPS result suggested that the Co/$Fe_{0.2}$-ZIF catalyst undergoes a rapid charge transformation of elemental species during the activated process. The hybridized Co/Fe species rapidly oxidized and transformed the catalytic sites into a higher valence state, producing excellent OER catalytic activity. Nevertheless, the activated Co/$Fe_{0.2}$-ZIF was further characterized and revealed that the crystal structure is significantly changed compared to the fresh Co/$Fe_{0.2}$-ZIF. The identical diffraction of ZIF peaks disappeared on activated Co/$Fe_{0.2}$-ZIF (Fig. 5(c)), which implies the decomposition of their crystalline after a long time chrono-potential test. The carbon peak from the carbon paper at 26.6° was mainly maintained on activated Co/$Fe_{0.2}$-ZIF without other species peaks. A similar result was observed via Fourier transform infrared (FT-IR) spectroscopy (Fig. 5(d)). The peaks at both 1204.55 and 1148.59 cm^{-1} represent the characteristic peaks of C–O bonding, which further suggests the existence of an oxidized phase of metal on activated Co/$Fe_{0.2}$-ZIF. The activated catalyst before reaction resulted in disorder coordination or collapsed structure of the ZIF catalysts to transform into active species. The metal structure of Co/Fe was transferred into a new metal-oxide species and was well-dispersed on carbon paper, which enhanced the exposure of more active sites.

In order to identify the true active sites and roles of Co/Fe-ZIF in OER, DFT calculations were conducted to further investigate and understand the catalytic mechanism of OER. The simulation models of Co/Fe-ZIF and ZIF-67 are shown in Figs. S10 and S11 in the ESM. The reaction pathways of intermediate substances OH*, O* and OOH* are shown in Fig. 6(a), which are used for each basic step of OER on Co/Fe-ZIF. In order to determine the rate determining step and explore the true active sites, the free energies of ZIF-67 and Co/Fe-ZIF intermediates (OH*, O* and OOH*) in the OER process were calculated using the DFT method, as shown in Fig. 6(b). The rate-determining step (RDS) was determined based on the maximum change in ΔG (ΔG represents Gibbs free energy), with the formation of OOH* found to be the RDS of OER for all systems. Compared with ZIF-67, the RDS of Co/Fe-ZIF has a smaller energy barrier of 1.15 eV. These results all demonstrate that when a Co atom is replaced by a Fe atom, the adsorption of OH*, O* and OOH* is enhanced, which is consistent with the experimental results.

4 Conclusions

The hybridized iron and cobalt atoms in the crystalline ZIF (Co/Fe-ZIF) was achieved by the straightforward of SST method. The simple approach to hybrid iron and cobalt in framework structure like ZIF-67 provided the unique structural characteristics and the charge rearrangement that significantly affected their catalytic performance for OER. The characterization of Co/Fe-ZIF catalysts revealed that the incorporated iron and its content showed a significant result in the OER performance. The synergy iron and

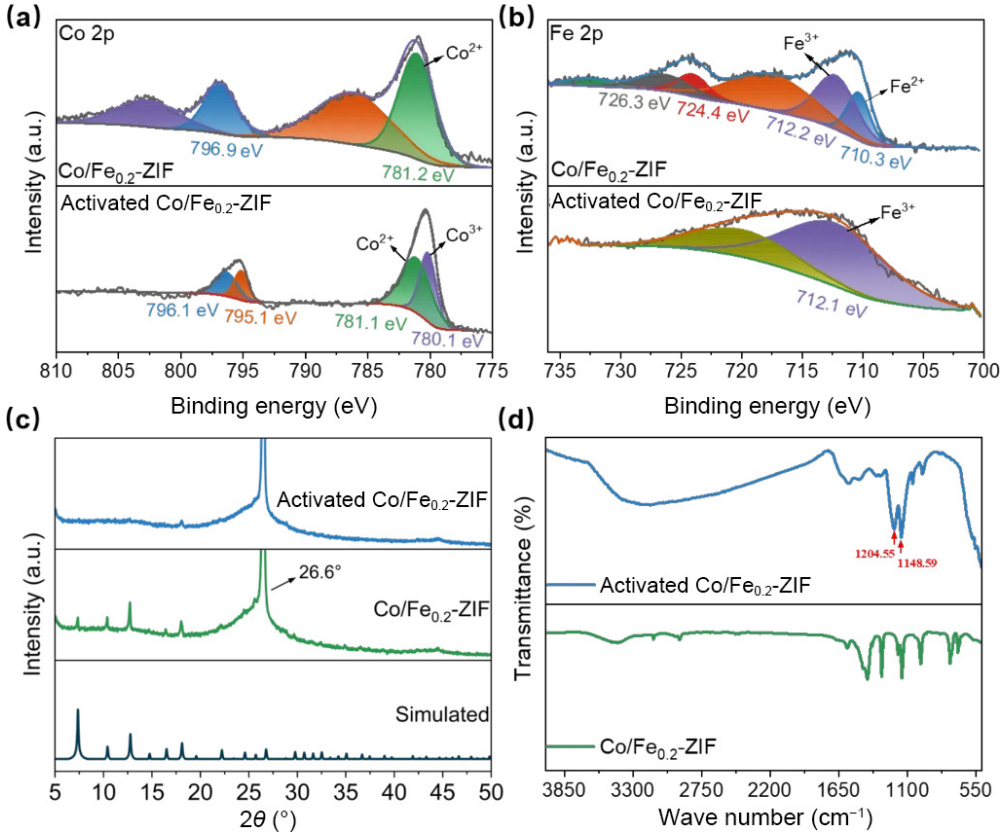

Figure 5 XPS of as-synthesized and activated Co/Fe$_{0.2}$-ZIF: (a) Co 2p and (b) Fe 2p. (c) XRD patterns of Co/Fe$_{0.2}$-ZIF before and after OER. (d) Infrared spectrum of Co/Fe$_{0.2}$-ZIF before and after OER.

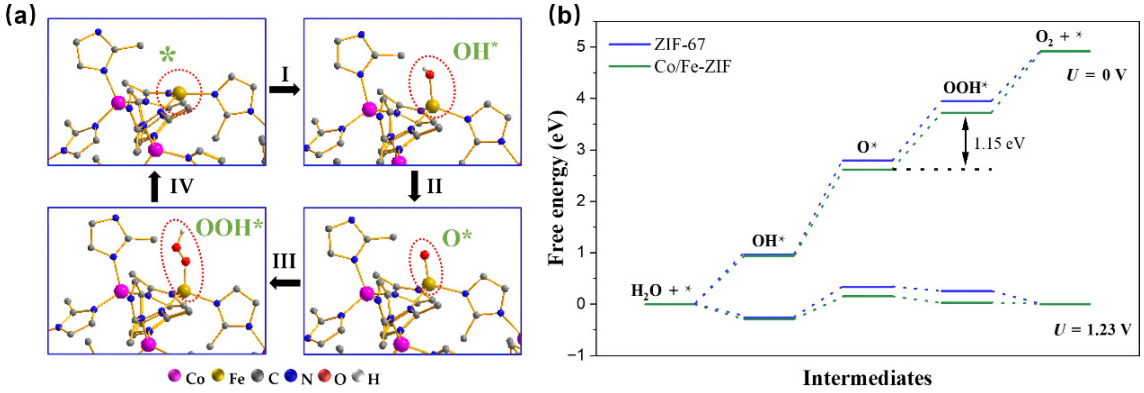

Figure 6 (a) Elementary reaction steps of the OER process on the Co/Fe-ZIF with the intermediates (OH*, O* and OOH*). (b) The Gibbs free energy profile of Co/Fe-ZIF and ZIF-67 for H_2O, OH*, O*, OOH* and O_2. *U* represents the internal energy.

cobalt atom triggers to promote the easy-transform into active species and transfer of orbital electrons from Co to Fe, resulting in excellent OER catalytic activity. At a current density of 10 mA·cm^{-2} in 1 M KOH, the Co/Fe$_{0.2}$-ZIF catalyst exhibited the lowest overpotential of 285 mV, surpassing the non-iron functional catalyst of ZIF-67 (380 and 369 mV). Importantly, compared to the commercial RuO_2 catalyst (311 mV), the Co/Fe$_{0.2}$-ZIF catalyst provided a lower overpotential, demonstrating that synergy iron significantly improved the high-efficiency Co/Fe$_{0.2}$-ZIF electrocatalyst. Finally, this development of non-noble metal hybridized Co/Fe-ZIF catalyst through the SST method provides a new pathway for straightforward preparing hybridized metals electrocatalysts based on ZIFs which opens the possibility for synthesis of multi-metals decoration in the catalyst and large-scale catalysts for practical use as electrocatalysts for OER.

Electronic Supplementary Material: Supplementary material (the overpotential comparison, the electrolyte before and after reaction, CVs collected at various scan rates, crystal diffraction pattern of materials, X-ray photoelectron spectroscopy, crystal morphology (SEM), the simulation models of Co/Fe-ZIF and diagram of drainage experiment) is available in the online version of this article at https://doi.org/10.26599/NR.2025.94907022.

Data availability

All data needed to support the conclusions in the paper arepresented in the manuscript and/or the Electronic Supplementary Material. Additional data related to this paper may be requested from the corresponding author upon request.

Acknowledgements

The authors are grateful to the State Key Lab of Advanced Technology for Materials Synthesis and Processing for financial support (Wuhan University of technology). S. C. appreciates the National Natural Science Foundation of China (No. 21950410754).

Declaration of competing interest

All the contributing authors report no conflict of interests in this work.

Author contribution statement

Y. S. X.: Supervision, investigation. Z. H. L.: Investigation, methodology, data curation, formal analysis, software, writing – original draft. Z. H. C.: Investigation, methodology, data curation, formal analysis, software, DFT calculation. S. C.: Conceptualization, methodology, data curation, visualization, formal analysis, supervision, writing – review & editing. All the authors have approved the final manuscript.

Use of AI statement

None.

References

[1] Chai, G. L.; Qiu, K. P.; Qiao, M.; Titirici, M. M.; Shang, C. X.; Guo, Z. X. Active sites engineering leads to exceptional ORR and OER bifunctionality in P, N Co-doped graphene frameworks. *Energy Environ. Sci.* **2017**, *10*, 1186–1195.

[2] Chen, F. Y.; Wu, Z. Y.; Adler, Z.; Wang, H. T. Stability challenges of electrocatalytic oxygen evolution reaction: From mechanistic understanding to reactor design. *Joule* **2021**, *5*, 1704–1731.

[3] Chen, P. Z.; Hu, X. L. High-efficiency anion exchange membrane water electrolysis employing non-noble metal catalysts. *Adv. Energy Mater.* **2020**, *10*, 2002285.

[4] Du, L.; Luo, L. L.; Feng, Z. X.; Engelhard, M.; Xie, X. H.; Han, B. H.; Sun, J. M.; Zhang, J. H.; Yin, G. P.; Wang, C. M. et al. Nitrogen-doped graphitized carbon shell encapsulated NiFe nanoparticles: A highly durable oxygen evolution catalyst. *Nano Energy* **2017**, *39*, 245–252.

[5] Li, X. Z.; Fang, Y. Y.; Lin, X. Q.; Tian, M.; An, X. C.; Fu, Y.; Li, R.; Jin, J.; Ma, J. T. MOF derived Co_3O_4 nanoparticles embedded in N-doped mesoporous carbon layer/MWCNT hybrids: Extraordinary bi-functional electrocatalysts for OER and ORR. *J. Mater. Chem. A* **2015**, *3*, 17392–17402.

[6] Lai, C. G.; Liu, X. B.; Cao, C. Q.; Wang, Y.; Yin, Y. H.; Liang, T. X.; Dionysiou, D. D. Structural regulation of N-doped carbon nanocages as high-performance bifunctional electrocatalysts for rechargeable Zn-air batteries. *Carbon* **2021**, *173*, 715–723.

[7] Park, Y. S.; Park, Y.; Jang, M. J.; Lee, J.; Kim, C.; Park, M. G.; Yang, J. C.; Choi, J.; Lee, H. M.; Choi, S. M. Effect of intrinsic and extrinsic activity of electrocatalysts on anion exchange membrane water electrolyzer. *Chem. Eng. J.* **2023**, *472*, 145150.

[8] Wu, L. H.; Guan, Z. X.; Guo, D. Y.; Yang, L.; Chen, X.; Wang, S. High-efficiency oxygen evolution reaction: Controllable reconstruction of surface interface. *Small* **2023**, *19*, 2304007.

[9] Chen, B. Y.; Biancolli, A. L. G.; Radford, C. L.; Holdcroft, S. Stainless steel felt as a combined OER electrocatalyst/porous transport layer for investigating anion-exchange membranes in water electrolysis. *ACS Energy Lett.* **2023**, *8*, 2661–2667.

[10] Ham, K.; Hong, S.; Kang, S.; Cho, K.; Lee, J. Extensive active-site formation in trirutile $CoSb_2O_6$ by oxygen vacancy for oxygen evolution reaction in anion exchange membrane water splitting. *ACS Energy Lett.* **2021**, *6*, 364–370.

[11] Pi, Y. C.; Qiu, Z. M.; Sun, Y. Y.; Ishii, H.; Liao, Y. F.; Zhang, X. Y.; Chen, H. Y.; Pang, H. Synergistic mechanism of sub-nanometric Ru clusters anchored on tungsten oxide nanowires for high-efficient bifunctional hydrogen electrocatalysis. *Adv. Sci.* **2023**, *10*, 2206096.

[12] Saad, A.; Liu, D. Q.; Wu, Y. C.; Song, Z. Q.; Li, Y.; Najam, T.; Zong, K.; Tsiakaras, P.; Cai, X. K. Ag nanoparticles modified crumpled borophene supported Co_3O_4 catalyst showing superior oxygen evolution reaction (OER) performance. *Appl. Catal. B: Environ.* **2021**, *298*, 120529.

[13] Nandi, S.; Singh, S. K.; Mullangi, D.; Illathvalappil, R.; George, L.; Vinod, C. P.; Kurungot, S.; Vaidhyanathan, R. Low band gap benzimidazole COF supported Ni_3N as highly active OER catalyst. *Adv. Energy Mater.* **2016**, *6*, 1601189.

[14] Li, X. R.; Li, Y. P.; Wang, C. L. A 3D hierarchical electrocatalyst: Core–shell Cu@$Cu(OH)_2$ nanorods/MOF octahedra supported on N-doped carbon for oxygen evolution reaction. *Nano Res.* **2023**, *16*, 8012–8017.

[15] Mo, F.; Zhou, Q. X.; Wang, Q.; Hou, Z. L.; Wang, J. L. The applications of MOFs related materials in photo/electrochemical decontamination: An updated review. *Chem. Eng. J.* **2022**, *450*, 138326.

[16] Qian, Y. T.; Zhang, F. F.; Pang, H. A review of MOFs and their composites-based photocatalysts: Synthesis and applications. *Adv. Funct. Mater.* **2021**, *31*, 2104231.

[17] Wang, K. C.; Li, Y. P.; Xie, L. H.; Li, X. Y.; Li, J. R. Construction and application of base-stable MOFs: A critical review. *Chem. Soc. Rev.* **2022**, *51*, 6417–6441.

[18] Huang, Y.; Chen, Y. C.; Xu, M. J.; Ly, A.; Gili, A.; Murphy, E.; Asset, T.; Liu, Y. C.; De Andrade, V.; Segre, C. U. et al. Catalysts by pyrolysis: Transforming metal-organic frameworks (MOFs) precursors into metal-nitrogen-carbon (M-N-C) materials. *Mater. Today* **2023**, *69*, 66–78.

[19] Liu, J. L.; Zhu, D. D.; Guo, C. X.; Vasileff, A.; Qiao, S. Z. Design strategies toward advanced MOF-derived electrocatalysts for energy-conversion reactions. *Adv. Energy Mater.* **2017**, *7*, 1700518.

[20] Chaemchuen, S.; Kou, Z. K. Chapter 9—Recent development in metal-organic frameworks and their derivatives for electrocatalysis and fuel cells. In *Metal Organic Frameworks and Their Derivatives for Energy Conversion and Storage*. Guan, C., Ed.; Elsevier: Amsterdam, 2024; pp 187–220.

[21] Wei, Y.; Zheng, M. B.; Zhu, W.; Zhang, Y.; Hu, W. H.; Pang, H. Preparation of hierarchical hollow CoFe Prussian blue analogues and its heat-treatment derivatives for the electrocatalyst of oxygen evolution reaction. *J. Colloid Interface Sci.* **2023**, *631*, 8–16.

[22] Suryanto, B. H. R.; Wang, Y.; Hocking, R. K.; Adamson, W.; Zhao, C. Overall electrochemical splitting of water at the heterogeneous interface of nickel and iron oxide. *Nat. Commun.* **2019**, *10*, 5599.

[23] Shahzad, A.; Zulfiqar, F.; Nadeem, M. A. Cobalt containing bimetallic ZIFs and their derivatives as OER electrocatalysts: A critical review. *Coord. Chem. Rev.* **2023**, *477*, 214925.

[24] Zhang, Y.; Lu, J. D.; Zhang, G. X.; Zhu, R. M.; Pang, H. Ternary alloy and metal oxides embedded in yolk–shell polyhedrons as bifunctional oxygen electrocatalyst. *Rare Met.* **2024**, *43*, 478–488.

[25] Dymerska, A.; Środa, B.; Sielicki, K.; Leniec, G.; Zielińska, B.; Zairov, R.; Nazmutdinov, R.; Mijowska, E. Robust and highly efficient electrocatalyst based on ZIF-67 and Ni^{2+} dimers for oxygen evolution reaction: *In situ* mechanistic insight. *J. Energy Chem.* **2023**, *86*, 263–276.

[26] Feng, J. X.; Xu, H.; Dong, Y. T.; Ye, S. H.; Tong, Y. X.; Li, G. R. Corrigendum: FeOOH/Co/FeOOH hybrid nanotube arrays as high-performance electrocatalysts for the oxygen evolution reaction. *Angew. Chem., Int. Ed.* **2019**, *58*, 14795–14795.

[27] Feng, W. H.; Liu, C. L.; Zhang, G. X.; Yang, H.; Su, Y. C.; Sun, Y. Y.; Pang, H. Tuning the local coordination environment of single-atom catalysts for enhanced electrocatalytic activity. *EnergyChem* **2024**, *6*, 100119.

[28] Lee, S.; Moysiadou, A.; Chu, Y. C. Tracking high-valent surface iron

species in the oxygen evolution reaction on cobalt iron (oxy)hydroxides. *Energy Environ. Sci.* **2022**, *15*, 206–214.
[29] Wen, D.; Ma, Y.; Mu, G. M.; Huang, Q. P.; Luo, X. F.; Lin, D. M.; Xu, C. G.; Xie, F. Y.; Wang, G. Z.; Guo, W. H. Constructing MIL-53(Fe)@ZIF-67(Co) binary metal-organic framework hierarchical heterostructure electrodes for efficient oxygen evolution. *Dalton Trans.* **2023**, *52*, 10662–10671.
[30] Han, D. Y.; Hao, L.; Wang, R.; Gao, Y. J.; Su, M.; Zhang, Y. F. Design yolk–shelled FeCo layered double hydroxide via a "one-stone-two-birds" strategy for oxygen evolution reaction. *Sep. Purif. Technol.* **2024**, *336*, 126363.
[31] Pan, Y. D.; Zhang, J. S.; Zhao, Z. L.; Shi, L.; Wu, B. K.; Zeng, L. Iron-doped metal-organic framework with enhanced oxygen evolution reaction activity for overall water splitting. *Int. J. Hydrogen Energy* **2021**, *46*, 34565–34573.
[32] Shi, G. Y.; Xu, W.; Wang, J. C.; Klomkliang, N.; Mousavi, B.; Chaemchuen, S. Thermochemical transformation in the single-step synthesis of zeolitic imidazole frameworks under solvent-free conditions. *Dalton Trans.* **2020**, *49*, 2811–2818.
[33] Wang, J. C.; Chaemchuen, S.; Klomkliang, N.; Verpoort, F. *In situ* thermal solvent-free synthesis of zeolitic imidazolate frameworks with high crystallinity and porosity for effective adsorption and catalytic applications. *Cryst. Growth Des.* **2021**, *21*, 5349–5359.
[34] Zheng, Z. H.; Wang, J. C.; Liu, M.; Mousavi, B.; Liu, N.; Chaemchuen, S. Facile and green synthesis cobalt embedded in N-doped porous carbon under zeo-waste conditions as an efficient oxygen evolution reduction catalyst. *Microporous Mesoporous Mater.* **2022**, *337*, 111916.
[35] Niu, S.; Jiang, W. J.; Wei, Z. X.; Tang, T.; Ma, J. M.; Hu, J. S.; Wan, L. J. Se-doping activates FeOOH for cost-effective and efficient electrochemical water oxidation. *J. Am. Chem. Soc.* **2019**, *141*, 7005–7013.
[36] Tao, L.; Lin, C. Y.; Dou, S.; Feng, S.; Chen, D. W.; Liu, D. D.; Huo, J.; Xia, Z. H.; Wang, S. Y. Creating coordinatively unsaturated metal sites in metal-organic-frameworks as efficient electrocatalysts for the oxygen evolution reaction: Insights into the active centers. *Nano Energy* **2017**, *41*, 417–425.
[37] Tang, Y.; Zou, Z. J.; Wu, X. G.; Zuo, P. F.; Wang, L.; Huang, G. W.; Zhu, J.; Zhong, S. L. ZIF-67@POM hybrid-derived unique willow-shaped two-dimensional Mo-CoP nanostructures as efficient electrocatalysts for the oxygen evolution reaction. *New J. Chem.* **2023**, *47*, 9887–9893.
[38] Li, S. S.; Gao, Y. Q.; Li, N.; Ge, L.; Bu, X. H.; Feng, P. Y. Transition metal-based bimetallic MOFs and MOF-derived catalysts for electrochemical oxygen evolution reaction. *Energy Environ. Sci.* **2021**, *14*, 1897–1927.
[39] Gu, X. C.; Wu, C. G.; Wang, S. L.; Feng, L. G. Cobalt fluoride/nitrogen-doped carbon derived from ZIF-67 for oxygen evolution reaction. *Catal. Commun.* **2022**, *162*, 106394.
[40] Jung, S.; Senthil, R. A.; Moon, C. J.; Tarasenka, N.; Min, A.; Lee, S. J.; Tarasenko, N.; Choi, M. Y. Mechanistic insights into ZIF-67-derived Ir-doped Co_3O_4@N-doped carbon hybrids as efficient electrocatalysts for overall water splitting using *in situ* Raman spectroscopy. *Chem. Eng. J.* **2023**, *468*, 143717.
[41] Zhu, R. M.; Ding, J. W.; Xu, Y. X.; Yang, J. P.; Xu, Q.; Pang, H. π-Conjugated molecule boosts metal-organic frameworks as efficient oxygen evolution reaction catalysts. *Small* **2018**, *14*, 1803576.
[42] Guo, X. Z.; Liang, G. Z.; Gu, A. J. Designed formation of CoS_2 nanoboxes with enhanced oxygen evolution reaction electrocatalytic properties. *Int. J. Hydrogen Energy* **2019**, *44*, 31020–31028.
[43] Zha, Q. Q.; Xu, W. Y.; Li, X. L.; Ni, Y. H. Chlorine-doped α-$Co(OH)_2$ hollow nano-dodecahedrons prepared by a ZIF-67 self-sacrificing template route and enhanced OER catalytic activity. *Dalton Trans.* **2019**, *48*, 12127–12136.
[44] Jia, H. X.; Zhang, M. Z.; Meng, T. J.; An, S. Y.; Wang, H.; Yang, X. J.; Zhang, Y. F. Facile synthesis of Fe, Co bimetal embedded nanoporous carbon polyhedron composites for an efficient oxygen evolution reaction. *J. Colloid Interface Sci.* **2020**, *563*, 189–196.
[45] Lashgari, S. M.; Yari, H.; Mahdavian, M.; Ramezanzadeh, B.; Bahlakeh, G.; Ramezanzadeh, M. Synthesis of graphene oxide nanosheets decorated by nanoporous zeolite-imidazole (ZIF-67) based metal-organic framework with controlled-release corrosion inhibitor performance: Experimental and detailed DFT-D theoretical explorations. *J. Hazard. Mater.* **2021**, *404*, 124068.
[46] Li, H. X.; Yao, Y. Z.; Zhang, J.; Du, J.; Xu, S. D.; Wang, C. H.; Zhang, D.; Tang, J. H.; Zhao, H. T.; Zhou, J. Degradation of phenanthrene by peroxymonosulfate activated with bimetallic metal-organic frameworks: Kinetics, mechanisms, and degradation products. *Chem. Eng. J.* **2020**, *397*, 125401.
[47] Li, J. X.; Fan, L. L.; Hua, Q. F.; Geng, Q. H.; Zhang, Y. Y.; Fan, X. L.; Ma, L.; Wang, C. M.; Zhu, W.; Feng, X. et al. Ordered macroporous carbonous skeletons implanted with dual-phase Co/CoFe nanoparticles for boosting electrocatalytic performance. *Chem. Eng. J.* **2023**, *470*, 144399.
[48] Zhang, H.; Zhong, J.; Zhou, G. X.; Wu, J. L.; Yang, Z. Y.; Shi, X. M. Microwave-assisted solvent-free synthesis of Zeolitic Imidazolate framework-67. *J. Nanomater.* **2016**, *2016*, 9648386.
[49] Zhou, Q. Y.; Zhang, Z.; Cai, J. J.; Liu, B.; Zhang, Y. L.; Gong, X. F.; Sui, X.; Yu, A. P.; Zhao, L.; Wang, Z. B. et al. Template-guided synthesis of Co nanoparticles embedded in hollow nitrogen doped carbon tubes as a highly efficient catalyst for rechargeable Zn-air batteries. *Nano Energy* **2020**, *71*, 104592.
[50] Qian, Q. Z.; Li, Y. P.; Liu, Y.; Yu, L.; Zhang, G. Q. Ambient fast synthesis and active sites deciphering of hierarchical foam-like trimetal-organic framework nanostructures as a platform for highly efficient oxygen evolution electrocatalysis. *Adv. Mater.* **2019**, *31*, 1901139.
[51] Li, J. T. Oxygen evolution reaction in energy conversion and storage: Design strategies under and beyond the energy scaling relationship. *Nano-Micro Lett.* **2022**, *14*, 112.
[52] Ge, K.; Sun, S. J.; Zhao, Y.; Yang, K.; Wang, S.; Zhang, Z. H.; Cao, J. Y.; Yang, Y. F.; Zhang, Y.; Pan, M. W. et al. Facile synthesis of two-dimensional iron/cobalt metal-organic framework for efficient oxygen evolution electrocatalysis. *Angew. Chem., Int. Ed.* **2021**, *60*, 12097–12102.
[53] Hou, X. B.; Han, Z. K.; Xu, X. J.; Sarker, D.; Zhou, J.; Wu, M.; Liu, Z. C.; Huang, M. H.; Jiang, H. Q. Controllable amorphization engineering on bimetallic metal-organic frameworks for ultrafast oxygen evolution reaction. *Chem. Eng. J.* **2021**, *418*, 129330.
[54] Chen, C. L.; Sun, M. Z.; Zhang, F.; Li, H. J.; Sun, M. R.; Fang, P.; Song, T. L.; Chen, W. X.; Dong, J. C.; Rosen, B. et al. Adjacent Fe site boosts electrocatalytic oxygen evolution at Co site in single-atom-catalyst through a dual-metal-site design. *Energy Environ. Sci.* **2023**, *16*, 1685–1696.
[55] Li, P.; Qiang, F. Q.; Tan, X. H.; Li, Z.; Shi, J.; Liu, S.; Huang, M. H.; Chen, J. W.; Tian, W. Q.; Wu, J. Y. et al. Electronic modulation induced by decorating single-atomic Fe-Co pairs with Fe-Co alloy clusters toward enhanced ORR/OER activity. *Appl. Catal. B: Environ.* **2024**, *340*, 123231.
[56] Tang, T. M.; Han, J. Y.; Wang, Z. L.; Niu, X. D.; Guan, J. Q. Diatomic Fe-Co catalysts synergistically catalyze oxygen evolution reaction. *Nano Res.* **2024**, *17*, 3794–3800.
[57] Chen, J. D.; Zheng, F.; Zhang, S. J.; Fisher, A.; Zhou, Y.; Wang, Z. Y.; Li, Y. Y.; Xu, B. B.; Li, J. T.; Sun, S. G. Interfacial Interaction between FeOOH and Ni-Fe LDH to modulate the local electronic structure for enhanced OER electrocatalysis. *ACS Catal.* **2018**, *8*, 11342–11351.